Large Anomalous and Topological Hall Effect and Nernst Effect in a Dirac Kagome Magnet Fe_3Ge

Chunqiang Xu[1,2], Shuvankar Gupta[2], Hengxin Tan[3], Hyeonhu Bae[3], Oluwatobiloba Olajumoke[2], Mingyu Xu[4], Yan Wu[5], Xiaofeng Xu[6], Pengpeng Zhang[2], Weiwei Xie[4], Binghai Yan[3], Xianglin Ke[2]

[1] *School of Physical Science and Technology, Ningbo University, Ningbo 315211, China*
[2]*Department of Physics and Astronomy, Michigan State University, East Lansing, Michigan 48824, USA*
[3]*Department of Condensed Matter Physics, Weizmann Institute of Science, Rehovot, Israel*
[4]*Department of Chemistry, Michigan State University, East Lansing, Michigan 48824, USA*
[5]*Neutron Scattering Division, Oak Ridge National Laboratory, Oak Ridge, Tennessee 37831, USA*
[6]*Department of Applied Physics, Zhejiang University of Technology, Hangzhou 310023, China*

Searching for Kagome magnets with novel magnetic and electronic properties has been attracting significant efforts recently. Here, we report magnetic, electronic and thermoelectric properties of Fe_3Ge single crystals with Fe atoms forming a slightly distorted Kagome lattice. We showed that Fe_3Ge exhibits large anomalous Hall effect and anomalous Nernst effect. The observed anomalous transverse thermoelectric conductivity $|\alpha_{xz}^{A}|$ reaches ~ 4.6 A m^{-1} K^{-1}, which is larger than the conventional ferromagnets and most of topological ferromagnets reported in literature. Our first-principles calculations suggest that these exceptional transport properties are dominated by the intrinsic mechanism, which highlights the significant contribution of the Berry curvature of massive Dirac gaps in the momentum space. Additionally, a topological Hall resistivity of 0.9 $\mu\Omega$ cm and a topological Nernst coefficient of 1.2 μV/K were also observed, which are presumably ascribed to the Berry phase associated with the field-induced non-zero scalar spin chirality. These features highlight the synergic effects of the Berry phases in both momentum space and real space of Fe_3Ge, which renders it an excellent candidate for room-temperature thermoelectric applications based on transverse transport.

Magnetic Kagome lattice, which is composed of corner-sharing triangles of magnetic ions, gives rise to a rich variety of electronic and magnetic properties[1-11]. The complex interplay between spin, orbital, and lattice degrees of freedom in magnetic Kagome systems can lead to frustrated magnetism, topological states, and potentially novel quantum phases, etc. For instance, various compounds with a magnetic Kagome lattice have recently been reported to exhibit intriguing electronic properties, such as frustrated antiferromagnetic Gd_2PdSi_3 possessing a Skrymion lattice that gives rise to a giant topological Hall effect[12], ferrimagnetic $TbMn_6Sn_6$ with topological Chern magnetism[13-15], topological Dirac semimetal Fe_3Sn_2[16-18], ferromagnetic Weyl semimetal $Co_3Sn_2S_2$[19,20], and antiferromagnetic FeGe with charge-density wave (CDW) state[21,22], etc. In particular, magnets hosting topological Dirac fermions owing to the Kagome lattice tend to show anomalous transverse transport phenomena and have garnered intensive attention. Specifically, in ferromagnetic Kagome systems, when the Dirac cones are proximate to the Fermi level, the time-reversal symmetry breaking can induce an energy gap opening at the Dirac points. As a result, a significant Berry curvature emerges in the momentum space which can consequently generate an intrinsic anomalous Hall effect (AHE) and an anomalous Nernst effect (ANE, which refers to an induced electric voltage between two contact leads transverse to the applied thermal gradient along the longitudinal direction). For instance, a colossal ANE was observed in a topological ferromagnetic Kagome metal $UCo_{0.8}Ru_{0.2}Al$ with the Nernst effect coefficient reaching ~ a record value of 23 $\mu V/K$ [23]. Generally, the ANE is sensitive to the Berry curvature of electron bands near the Fermi level and is approximately proportional to the energy derivative of electric Hall conductivities at the Fermi level according to the Mott relationship[24-28].

Despite the novel properties of Kagome magnets hosting Dirac fermions, compounds with an ideal magnetic Kagome lattice that are suitable for room-temperature spintronic and thermoelectric applications remain scarce. This is due to the intrinsic coordination requirements of the magnetic Kagome lattice, which renders interatomic interactions highly sensitive to structural stability, with even minor perturbations capable of compromising its structural integrity. Very recently, by utilizing angle-resolved photoemission spectroscopy and density functional theory calculations, it was proposed

that Fe_3Ge, a ferromagnetic compound with an ordering temperature of ~ 660 K and a slightly distorted Kagome lattice, exhibits Dirac fermions[29]. And the topological nature of electronic properties has been supported by the observation of AHE[30,31] and topological Hall effect[31] in polycrystalline Fe_3Ge. Compared to polycrystalline samples, the absence of grain boundaries in single crystals offers an opportunity to investigate the intrinsic electronic and thermal transport properties. In addition, single crystals also enable the study of anisotropic electronic and magnetic properties, which are intimately correlated to the crystalline anisotropy. Therefore, it is desirable to investigate the electronic and thermoelectric properties of Fe_3Ge single crystals, which, in conjunction with theoretical calculations, allows for a more comprehensive understanding of the topological properties of this system.

In this paper, we report the key topological characteristics of electronic and thermoelectric transport properties in Fe_3Ge. We show that Fe_3Ge exhibits giant AHE and ANE. The observed anomalous thermoelectric transverse conductivity reaches ~ 4.6 A m^{-1} K^{-1}. Our first-principles calculations find several Dirac band crossings near the charge neutral point and reproduce qualitatively the observed AHE and ANE, indicating the intrinsic origin of the anomalous transport properties in Fe_3Ge and highlighting the importance of its topological electronic structure. In addition, a topological Hall resistivity with a value of ~ 0.9 $\mu\Omega$ cm and topological Nernst coefficient of ~ 1.2 μV/K were observed at 320 K, which is ascribable to the Berry curvature associated with the field-induced non-zero scalar spin chirality. These features, together with its high magnetic ordering temperature, place Fe_3Ge an ideal candidate for room-temperature thermoelectric applications based on Nernst effect.

Crystal structure and magnetic properties Figure 1A shows a photo image of Fe_3Ge rod-like single crystals grown using a Tin flux method. Fe_3Ge crystallizes in hexagonal $D0_{19}$ type structure with the space group $P6_3/mmc$ (No.194). The magnetic Fe ions form a Kagome plane with a non-magnetic Ge ion occupying at the center of each hexagon. Interestingly, as also detailed in the Supplemental Information, in Fe_3Ge the Fe atoms do not occupy the special positions at $x = 1/6$ and $y = 1/3$. As illustrated in Figure 1B, while six Fe ions still form a regular hexagon, the Ge ion is slightly off-center of

the hexagon, which results in $\gamma \neq \beta \neq \alpha = 60°$. Note that within each hexagon the two adjacent Fe-Fe bond lengths are 2.672 Å and 2.497 Å, indicating a slightly distorted magnetic Kagome lattice. Each Kagome plane is alternately stacked along the *c*-axis as shown in Figure 1C. Detailed single crystal X-ray characterizations, including four-circle single-crystal X-ray diffraction and the comprehensive structural analysis, as well as Laue diffraction measurements, are described in the Supplemental Information.[32]

Figure 1D shows the temperature dependence of magnetic susceptibility with the magnetic field applied along the *c*-axis and the *ab* plane respectively. Note that there is no difference in magnetic susceptibility between field-cooled and zero-field-cooled measurements. The system becomes ferromagnetically order below $T_c \sim 660$ K with the magnetic easy-axis aligned along the *c*-axis[33,34]. This is followed by a spin reorientation transition at $T_{SR} \sim 385$ K with the magnetic moment direction changed from the *c*-axis to the *ab* plane, which is evidenced by the sharp drop in magnetic susceptibility measured along the *c*-axis. The spin reorientation transition is supported by single-crystal neutron diffraction measurements. Figure 1E plots the temperature dependence of integrated neutron scattering intensity of (1 0 0) and (1 0 1) Bragg reflections, both of which include both nuclear and magnetic scattering intensity contribution. Note that neutrons couple to the magnetic moment perpendicular to the momentum transfer vector **q**. Thus, the decrease in the scattering intensity of (1 0 0) Bragg peak and the increase of (1 0 1) Bragg peak intensity below T_{SR} indicates the spin-orientation. The magnetic structures obtained by refining a series of Bragg peaks measured at 410 K and 360 K are illustrated in the insets of Figure 1E. At 410 K spins align along the *c*-axis, while at 360 K there is a large magnetic moment component (~ 1.93 u_B/Fe) lying within the *ab* plane and ~ 0.45 u_B/Fe along the *c*-axis, respectively. The refined total magnetic moment is ~ 1.98 u_B/Fe, which agrees with the value obtained from isothermal magnetization $M(H)$ measurements and from previous neutron powder diffraction measurements[33]. Figure 1F presents a typical $M(H)$ measured with $H \,//\, c$ and $H \,//\, ab$ at 300 K.

Resistivity and Hall conductivity Figure 2A shows the schematic diagram of the longitudinal resistivity, Hall effect, and thermoelectric measurements. For the longitudinal resistivity ρ_{zz}, as an example, both the electric current and longitudinal voltage are along

the z-axis. Figure 2B presents the temperature dependence of longitudinal resistivity ρ_{xx} and ρ_{zz}. Both ρ_{xx} and ρ_{zz} decrease with the decreasing temperature, with a large residual resistivity ratio (RRR) of ~ 20 and ~ 40 for in-plane and out-of-pane measurements, respectively, affirming the high quality of Fe_3Ge single crystals. Unlike most other Kagome materials, the value of the in-plane resistivity ρ_{xx} is about 3 ~ 4 times of the out-of-plane resistivity ρ_{zz} over the entire temperature range measured. Such an anisotropic electronic transport property presumably arises from the stronger orbital hybridization between neighboring 3d electrons of Fe ions due to shorter Fe-Fe bond length along the out-of-plane direction compared to that within the *ab* plane. Note that similar anisotropic character between ρ_{xx} and ρ_{zz} in Fe_3Ge has also been reported in Ref. [29] recently.

Figure 2C shows the magnetic field dependence of Hall resistivity $-\rho_{xz}$ measured at various temperatures, where an electrical current is applied along the longitudinal direction (c(z)-axis) and the magnetic field is along the perpendicular direction (ab-plane). To eliminate the Hall resistivity contribution from the voltage probe misalignment, all data measured at different temperatures were processed by $\rho_{xz} = (\rho_{xz}(+\mu_0 H) - \rho_{xz}(-\mu_0 H))/2$ since the Hall signal is antisymmetric relative to magnetic field. As expected for ferromagnetic metals, the Hall resistivity ρ_{xz} rapidly increases with the magnetic field and then saturates when the saturation magnetization is nearly reached, showing the AHE. Compared to the dominant AHE, the small slope at high magnetic field contributed by the ordinary Hall effect indicates that the ordinary Hall effect is negligible. The AHE value at 320 K is ~ $2\mu\Omega\, cm$, which is comparable with those reported in some well-known magnetic Kagome materials, e.g., $Co_3Sn_2S_2$ and Fe_3Sn_2[16,19].

To figure out the mechanism of the observed AHE in Fe_3Ge, we plot the scaling of $|\rho_{xz}|$ versus $\rho_{zz}\rho_{xx}$. As shown in Figure 2D, the good linear relation between $|\rho_{xz}|$ and $\rho_{zz}\rho_{xx}$ suggests that the extrinsic skew-scattering which generally gives $|\rho_{xz}| \propto (\rho_{zz}\rho_{xx})^{1/2}$ can be ruled out and the intrinsic Berry phase or extrinsic side-jump mechanisms are dominant in Fe_3Ge. In Figure 2E, we plot the magnetic field dependence of Hall conductivity σ_{xz}, which is defined as $\sigma_{xz} = \frac{-\rho_{xz}}{\rho_{xx}\rho_{zz} - \rho_{xz}\rho_{zx}}$, where $\rho_{zx} = -\rho_{xz}$. Because ρ_{xz} is much smaller than both ρ_{xx} and ρ_{zz} as shown in Figure 2B and 2C, σ_{xz}

thus can be approximated as $\sigma_{xz} \approx \frac{-\rho_{xz}}{\rho_{xx}\rho_{zz}}$. Theoretically, the extrinsic side-jump contribution of σ_{xz}^{A} has been shown to be on the order of $(e^2/(ha)(\varepsilon_{SO}/E_F))$, where e is electronic charge, h is the Plank constant, a is the lattice parameter, ε_{SO} is the spin-orbit coupling (SOC), the E_F is the Fermi energy[35]. For metallic ferromagnets, ε_{SO}/E_F is generally smaller than 10^{-2}. With $a \sim 4$ - 5 Å, the estimated extrinsic side-jump contribution is $\sim$ 2 $(\Omega^{-1}\mathrm{cm}^{-1})$, much smaller than the total σ_{xz}^{A}. This suggests that the AHE in Fe_3Ge is dominated by an intrinsic mechanism, which is supported by the theoretical calculation as to be discussed later. The temperature dependent σ_{xz}^{A} is presented in Figure 2F. With the increase of temperature, σ_{xz}^{A} first increases and then decreases, with $|\sigma_{xz}^{A}| \sim 350$ $(\Omega^{-1}\mathrm{cm}^{-1})$ at 60 K and a maximum $|\sigma_{xz}^{A}| \sim 550$ $(\Omega^{-1}\mathrm{cm}^{-1})$ at 220 K. The large anomalous Hall conductivity observed in Fe_3Ge is comparable to, or exceeds, those reported for other Kagome magnets such as Mn_3Sn[36], Mn_3Ge[3], Fe_3Sn_2 [16], $TbMn_6Sn_6$ [13,14], and $Co_3Sn_2S_2$ [19]. As to be discussed later, this highlights the strong Berry curvature contributions arising from the non-trivial topology of the electronic bands in Fe_3Ge. Note that during our manuscript preparation we noticed a very recent preprint[37] reporting the observation of a large anomalous Hall effect on Fe_3Ge single crystals, which however did not consider the anisotropic electronic transport between ρ_{xx} and ρ_{zz} in the data processing.

Seebeck and Nernst effect We investigated the thermoelectric transport properties of Fe_3Ge with the thermal gradient applied along the *z*-axis and the magnetic field along the *y*-axis, as illustrated by the schematics sketched in Figure 2A. Figure 3A presents the temperature dependence of Seebeck coefficient S_{zz} measured at zero applied magnetic field. The negative value of S_{zz} over the whole measurement temperature range indicates that the n-type (electron) charge carriers are dominant in Fe_3Ge. Figure 3B shows the magnetic field dependent Nernst signal S_{xz} measured at various temperatures. Similar to the Hall resistivity ρ_{xz} shown in Figure 2C, the Nernst signal S_{xz} is dominated by the anomalous contribution. The normal component of S_{xz} in the high field regime is negligible, as implied by the nearly field-independence of S_{xz}. It is noted that S_{xz} is ~ 3.2 μV/K at 320 K, which is much larger than those of isostructural antiferromagnets Mn_3X and conventional ferromagnets[2,38-40]. To better understand the thermoelectric properties of

Fe_3Ge, in Figure 3C we present the calculated transverse thermoelectric conductivity α_{xz} at various temperatures using $\alpha_{xz} = \frac{S_{xz}\rho_{zz} - \rho_{xz}S_{zz}}{\rho_{xx}\rho_{zz}}$ with ρ_{xx}, ρ_{zz}, ρ_{xz}, S_{zz}, S_{xz} being the measured quantities[41]. It is clearly seen that $\alpha_{xz}(H)$ behaves similar to $\rho_{xz}(H)$ and $S_{xz}(H)$ since both ρ_{xx} and S_{zz} barely depend on magnetic field. In Figure 3D we plot the temperature dependence of the anomalous component α_{xz}^{A} extracted at 2 T. α_{xz}^{A} increases with increasing temperature and tends to saturate at high temperature, reaching a value of 4.6 A m^{-1} K^{-1} at 300 K. Such behavior is significantly different from that of conventional ferromagnetic metals, where α_{xz}^{A} increases linearly with decreasing temperature and follows the temperature dependence of magnetization[42].

To better understand the origin of the AHE and ANE features observed in Fe_3Ge, we performed theoretical calculations to obtain the electronic structure, Berry curvature, anomalous Hall conductivity, and anomalous thermoelectric conductivity. Figure 3E shows the calculated electronic structure and the Berry curvature distribution. Without taking into account the spin-orbit coupling, multiple band crossings occur near the Fermi level, three of which are positioned exactly at the Fermi level along the Γ–M, Γ–K, and Γ–A directions. Spin-orbit coupling induces small gaps at these crossings, leading to significant Berry curvature, as shown in the Berry curvature distribution. Notably, the Berry curvature at the two edges of each gap exhibits opposite signs. This substantial Berry curvature gives rise to a large anomalous Hall conductivity, which strongly depends on the position of the Fermi Level as illustrated in the inset of Figure 2F. While the experimental AHE $|\sigma_{zx}^{A}|$ at 60 K is slightly smaller than the theoretical AHE at the charge neutral point E_0: $\sigma_{zx}^{A} \sim 400$ ($\Omega^{-1}\mathrm{cm}^{-1}$), it is closer to the calculated value at –15 meV or 35 meV relative to E_0.

The large Berry curvature near the Fermi level also enhances the ANE. Figure 3F shows the temperature dependence of α_{xz}^{A} at several representative chemical potentials, which was calculated using Kubo formula, $\alpha_{xy}^{int}(T) = -\frac{e}{\hbar}\int d\zeta \frac{\partial f(\zeta-\mu)}{\partial \zeta} \frac{\zeta-\mu}{T} \int_{BZ} \frac{d\vec{k}}{(2\pi)^3} \sum_{\epsilon_n<\zeta} \Omega_{xy}^{z}(\vec{k})$, wherein $f(\zeta-\mu) = \left(e^{\frac{\zeta-\mu}{k_B T}} + 1\right)$ is the Fermi-Dirac distribution function and μ is the chemical potential. As it shows, α_{xz}^{A} increases with increasing the temperature when the chemical potential is below about –50

meV (relative to the charge neutral point). The overall magnitude of α_{xz}^{A} is also comparable with the experimental values, affirming that the large α_{xz}^{A} is intrinsic and arises from the Berry curvature of the gapped bands near the crossings as shown in Figure 3E. Figure 3G presents the temperature dependence of $|\alpha_{xz}^{A}/\sigma_{xz}^{A}|$ ratio of Fe_3Ge and its comparison with other magnetic materials. While σ_{xz}^{A} is related to the Berry curvature of electronic bands over the whole Fermi sea and α_{xz}^{A} is sensitive to the Berry curvature of the electronic structure near the Fermi level, it was reported that this ratio shows a universal feature: approaching to zero at the low temperature limit but to $\frac{k_B}{e}$ = 86 (μV/K) at high temperature[41]. Indeed, as shown in Figure 3G, this ratio of Fe_3Ge increases with temperature and approaches to $\frac{k_B}{e}$ around room temperature, a feature similar to that observed in other topological materials such as Mn_3Ge and Co_2MnGa [41]. In Figure 3H we plot the maximum α_{xz}^{A} value of Fe_3Ge in comparison with some conventional ferromagnets and well-known topological ferromagnets[20,23,40,43-52], highlighting the large transverse thermoelectric effect in Fe_3Ge. This, together with the high magnetic ordering temperature, renders Fe_3Ge an excellent candidate with great potential for practical thermoelectric applications based on Nernst effect.

Topological Hall effect and topological Nernst effect In addition to the AHE and ANE, we also observe topological Hall effect (THE) and topological Nernst effect (TNE) in Fe_3Ge single crystals. In some systems with nontrivial spin structure, the THE may emerge together with the ordinary Hall effect and ANE within a certain magnetic field-temperature phase region[53,54]. That is, $\rho_{xz} = \rho_{xz}^{O} + \rho_{xz}^{A} + \rho_{xz}^{T} = R_0\mu_0 H + S_A\rho_{xx}\rho_{zz}M + \rho_{xz}^{T}$, where the R_0, $S_A\rho_{xx}\rho_{zz}$, and ρ_{xz}^{T} are the ordinary Hall coefficient, anomalous Hall coefficient, and the topological Hall resistivity, respectively. Thus, the ρ_{xz}^{T} can be calculated by subtracting both the ordinary and anomalous Hall components from the total Hall resistivity ρ_{xz}. At a fixed temperature, since both ρ_{xx} and ρ_{zz} are weakly field-dependent, ρ_{xz}^{A} effectively depends linearly on *M*. In Figure 4A, we overplot the $\rho_{xz}(H)$ and the scaled *M*(*H*) curves measured at 260 K with the magnetic field applied within the *ab* plane. Note that the magnetization and transport measurements were carried out on the exact same piece of single crystal sample to eliminate potential effects of different

demagnetization fields due to different sample geometries. The difference in the saturation fields of $M(H)$ and $\rho_{xz}(H)$ data, which was also observed in polycrystalline Fe_3Ge [31], implies the emergence of topological Hall effect in this system. Since the ordinary Hall component is much smaller than the other two components, the difference between total ρ_{xz} and ρ_{xz}^{A} (i.e., the scaled M term) gives ρ_{xz}^{T} which is represented by the green curves shown in Figure 4A (also see Fig. S2 and the related discussion in the Supplemental Information[32]). Following a similar approach, we can extract the TNE contribution from the total Nernst effect coefficient S_{xz} with $S_{xz} = S_0 + S_{xz}^{A} + S_{xz}^{T}$, where S_0, S_{xz}^{A}, and S_{xz}^{T} denote the ordinary ($\sim H$), anomalous ($\sim M$), and topological Nernst components, respectively. The green curve shown in Figure 4B represents the thus-extracted TNE S_{xz}^{T}. It is seen that both THE and TNE exhibit a maximum near 0.6 T, where the magnetization reaches ~ 90% of the saturated value (see Figure S3 and the related discussion in the Supplemental Information), implying the persistence of a residual non-collinear component. Upon further increasing the magnetic field, both THE and TNE signals decrease and approach to zero when the magnetization saturates at ~ 1.4 T. This suggests that the THE and TNE may arise from the magnetic field induced non-coplanar spin structure in Fe_3Ge, which gives non-zero spin chirality and thus non-zero Berry curvature. Figure 4C and 4D present the thus-extracted ρ_{xz}^{T} and S_{xz}^{T} at various temperatures, respectively, and Figure 4E and 4F show the corresponding magnetic field-temperature contour maps. Both ρ_{xz}^{T} and S_{xz}^{T} increase with temperature, reaching a value of 0.9 $\mu\Omega$ cm and 1.4 μV/K at 320 K, respectively, which are comparable to or surpass values of some related compounds, such as Fe_3Sn_2 [49], $ScMn_6Sn_6$ [55], MnGe [56], Gd_2PdSi_3 [57], $EuCd_2As_2$ [58], $Nd_3Ru_4Al_{12}$ [59], YMn_6Sn_6 [60,61], $ErMn_6Sn_6$ [62,63], Mn_5Si_3 [64], and Mn_3Ga [65]. Note that the THE was previously reported in Ref. [31] on the studies of Fe_3Ge polycrystalline samples but not in Ref. [30] and Ref. [37] on both polycrystalline and single crystalline samples.

The observation of the THE in Fe_3Ge, which has a collinear ferromagnetic structure at zero field, is intriguing. Generally, the emergence of the THE stems from non-zero static scalar spin chirality (SSC) in systems with non-coplanar spin texture (e.g, the formation of Skyrmion lattice) which induces a nontrivial real-space Berry phase and the associated fictitious magnetic field[53,54]. More recently, a fluctuation-driven mechanism has been

proposed to generate a finite SSC and account for the observation of THE in systems without static SSC (such as YMn_6Sn_6 [60] and Fe_3Ga_4 [66,67]), which involves chiral spin fluctuations. Although these materials exhibit a helical spin spiral ground state, it transitions—under an in-plane magnetic field—into a transverse conical spiral (TCS) phase, where the spiral propagates out-of-plane (along the c-axis) while spins rotate in the ab-plane. This TCS structure still lacks static scalar spin chirality yet enables the population of thermally excited chiral magnons with a preferred handedness. These magnons become unequally populated at finite temperature, dynamically generating a nonzero scalar spin chirality and giving rise to the THE[60,62,67]. As discussed previously, Fe_3Ge exhibits spin reorientation from the out-of-plane alignment above $T_{SR} \sim 385\ K$ to the in-plane alignment at lower temperatures, with zero-field neutron diffraction measurements revealing mixed in-plane and out-of-plane moment components near T_{SR} (Fig. 1E and Ref.[33]). This suggests that as the temperature approaches T_{SR}, the system's reduced anisotropy barriers may enable the formation of non-coplanar spin configurations in the presence of magnetic field, supported by recent first-principles predictions[31]. Very recent Lorentz Transmission Electron Microscopy measurements conducted at room temperature with in-plane applied magnetic fields reveal no evidence of Skyrmion spin textures in Fe_3Ge.[68] It is likely that the field-induced non-coplanar spin structure together with the chiral spin fluctuations gives rise to the observed THE in this system. Thus, future neutron scattering studies in the presence of magnetic field to probe the evolution of spin structure are highly desirable. It is worth pointing out that the THE and TNE peak position barely depends on the measurement temperature up to 320 K, as shown in Fig. 4(E,F). Although the underlying mechanism is still elusive, this feature is similar to the THE reported in YMn_6Sn_6 and $ErMn_6Sn_6$ in which the chiral spin fluctuations are found to be the driving mechanism of the observed THE [60,62]. On the other hand, for the chiral fluctuation driven topological Hall effect, it was shown that ρ^T at a constant field is proportional to temperature (i.e, $\rho^T \sim T$), as shown in Figure S4(c) for YMn_6Sn_6 [60]. The nearly linear temperature dependence of ρ_{xz}^T and S_{xz}^T of Fe_3Ge at 0.6 T shown in Figure S4 (a,b) implies that the topological Hall effect and topological Nernst effect in this system may be associated with chiral spin fluctuation driven non-zero scalar chirality as well.

In summary, we show that Fe_3Ge exhibits large anomalous Hall effect and anomalous Nernst effect with the anomalous Nernst conductivity reaching 4.6 A m^{-1} K^{-1}. Our first-principles calculations qualitatively reproduce the observed anomalous transverse transport results, highlighting the critical contribution from the Berry curvature of the massive Dirac gaps in the momentum space. In addition, both topological Hall effect and topological Nernst effect are also observed, with the topological Nernst coefficient increasing when the temperature approaches the spin-orientation phase transition, which presumably arises from the Berry phase associated with the field-induced non-zero scalar spin chirality. These results highlight the synergic effects of the Berry phases in both momentum space and real space of Fe_3Ge. This, in conjunction with its high magnetic ordering temperature, places this material a promising candidate for potential thermoelectric applications based on Nernst effect.

Acknowledgments S. G., O.E., and X.K. acknowledge the financial support by the U.S. Department of Energy, Office of Science, Office of Basic Energy Sciences, Materials Sciences and Engineering Division under Grant No. DE-SC0019259. The thermoelectric transport measurements were supported by National Science Foundation (DMR-2219046). M.X. and W.X. acknowledge the financial support by the U.S. Department of Energy, Office of Science, Office of Basic Energy Sciences, Materials Sciences and Engineering Division S under Contract DE-SC0023648. P. P. Zhang acknowledges the financial support from the U.S. Department of Energy, Office of Basic Energy Sciences, Division of Materials Sciences and Engineering under Award Number DE-SC0019120. Neutron diffraction part of this research used resources at the High Flux Isotope Reactor, a DOE Office of Science User Facility operated by the Oak Ridge National Laboratory. The beam time was allocated to DEMAND on proposal number IPTS-32305.1. C.X. was partially supported by the Start-up funds at Michigan State University and National Natural Science Foundation of China (Grants No. 12304071).

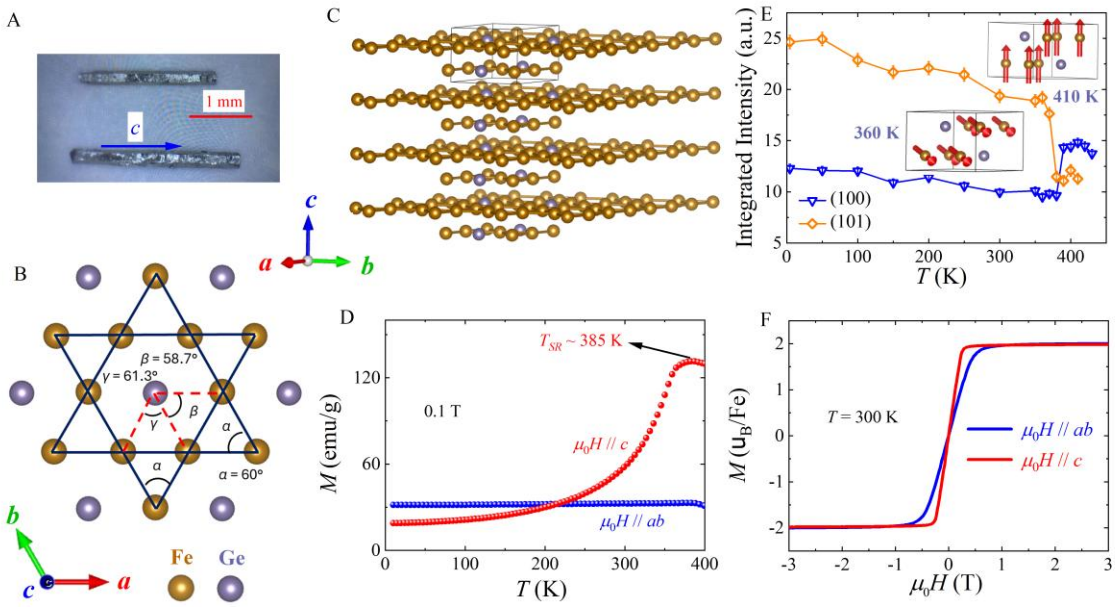

Figure 1: Crystal structure and magnetic properties. (A) An optical image of the as-grown Fe_3Ge single crystals. (B, C) Schematic view of the crystal structure of Fe_3Ge from two axes perspective, respectively. (D) Temperature dependence of magnetic susceptibility measured under 0.1 T. (E) The temperature dependence of integrated neutron scattering intensity of (100) and (101), the insets show the schematic diagram of spin configuration is indicated by red arrows at 360 K and 400 K. (F) The field dependence of magnetic susceptibility measured at 300 K.

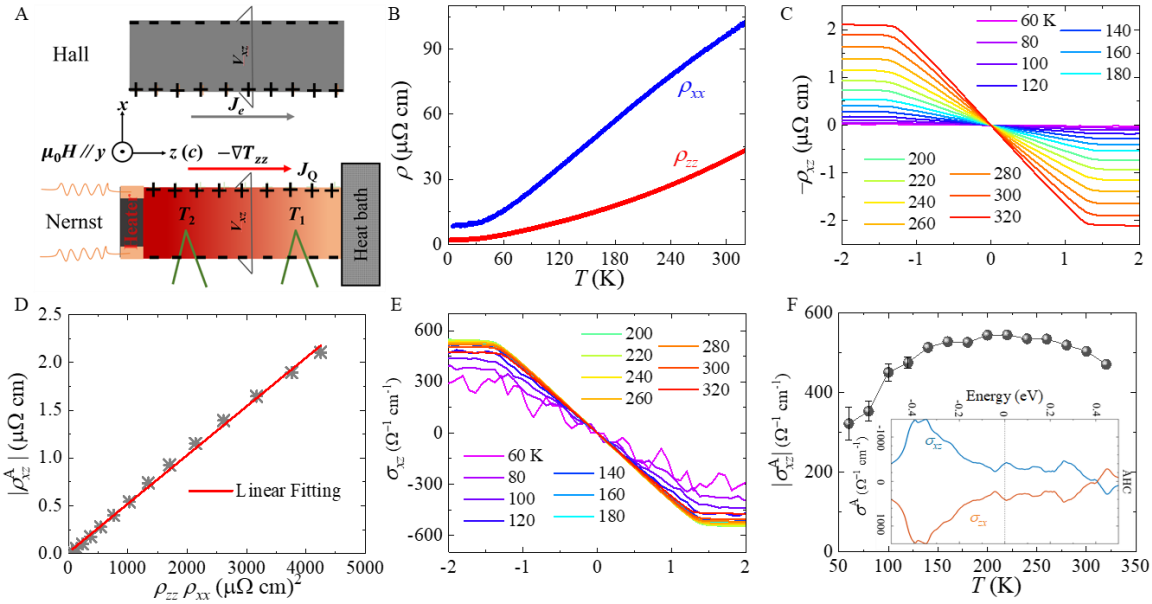

Figure 2: Anomalous Hall effect. (A) The schematic diagram of Hall effect and Nernst effect measurements. Note that $J_Q \parallel c$, $H \perp c$. (B) The temperature dependence of longitudinal resistivity ρ_{xx} and ρ_{zz} (C) The Hall resistivity ρ_{zx} at different temperatures. (D) Plot of ρ_{zx}^A vs $\rho_{xx}\rho_{zz}$, the red solid line is the linear fitting. (E) The Hall conductivity σ_{xz} at different temperatures. (F) The temperature dependence of experimental anomalous Hall conductivity $|\sigma_{xz}^A|$, the inset shows the theoretically calculated intrinsic σ_{xz}^A as a function of the chemical potential, where the magnetization is along one of the in-plane lattice vectors.

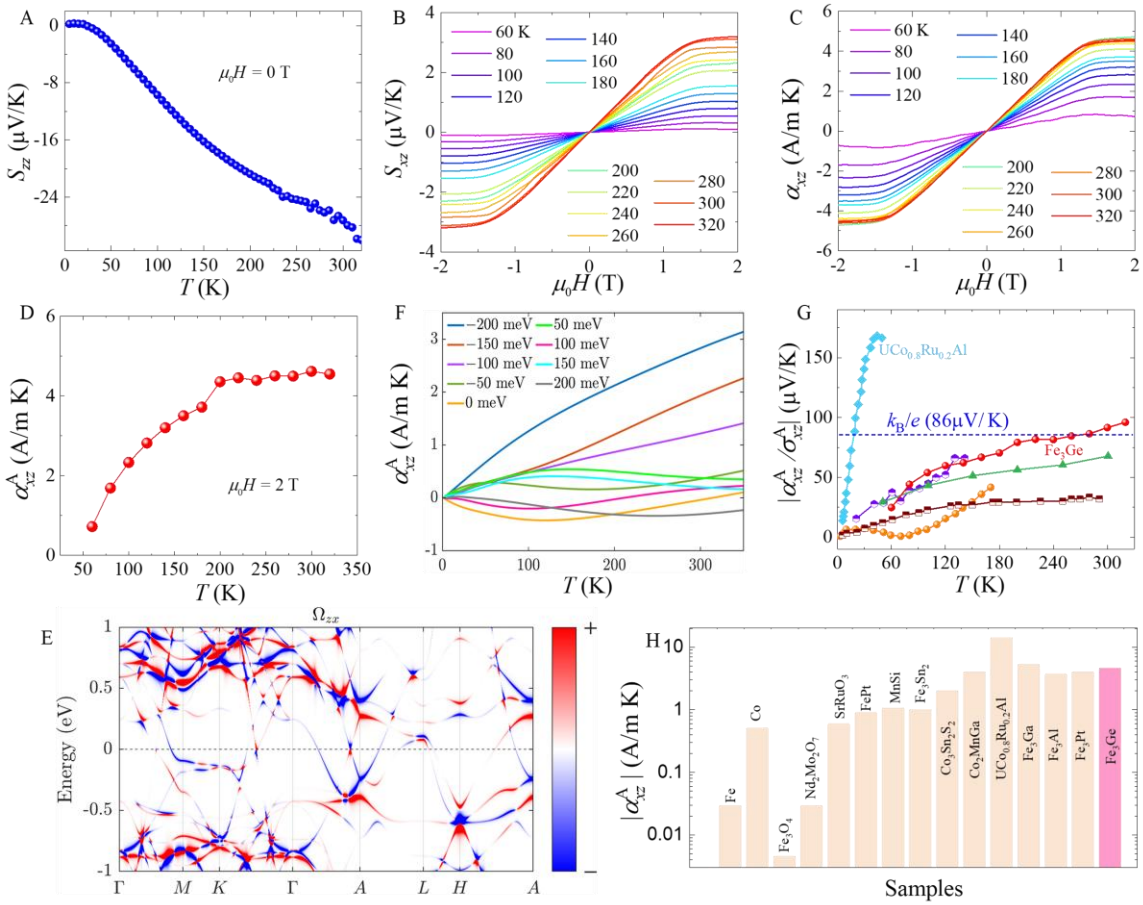

Figure 3: Anomalous transverse thermoelectric effect. (A) The temperature dependence of Seebeck coefficient S_{zz} under 0 magnetic field. (B) The Nernst signals as a function of field at different temperatures. (C) The magnetic field dependence of the calculated transverse thermoelectric conductivity α_{xz} using the five experimentally measured components ρ_{xx}, ρ_{zz}, ρ_{xz}, S_{zz}, S_{xz} at various temperatures. (D) The temperature dependence α^A_{xz} extracted from panel C at 2 T. (E) The electronic band structure and the projected Berry phase for bands near the Fermi energy. (F) The temperature dependence of the theoretically calculated α^A_{xz} at representative chemical potentials. (G) The ratio $|\alpha^A_{xz}/\sigma^A_{xz}|$ of Fe_3Ge as a function of temperature in comparison with other magnets[23]. (H) The value of $|\alpha^A_{xz}|$ of Fe_3Ge, compared with some well-known conventional ferromagnets and topological ferromagnets (Fe[50], Co[47], Fe_3O_4[40], $Nd_2Mo_2O_7$[45], $SrRuO_3$[43], $FePt$[48], $MnSi$[46], Fe_3Sn_2[49], $Co_3Sn_2S_2$[20], Co_2MnGa[44], $UCo_{0.8}Ru_{0.2}Al$[23], Fe_3Ga[51], Fe_3Al[51], and Fe_3Pt[52]).

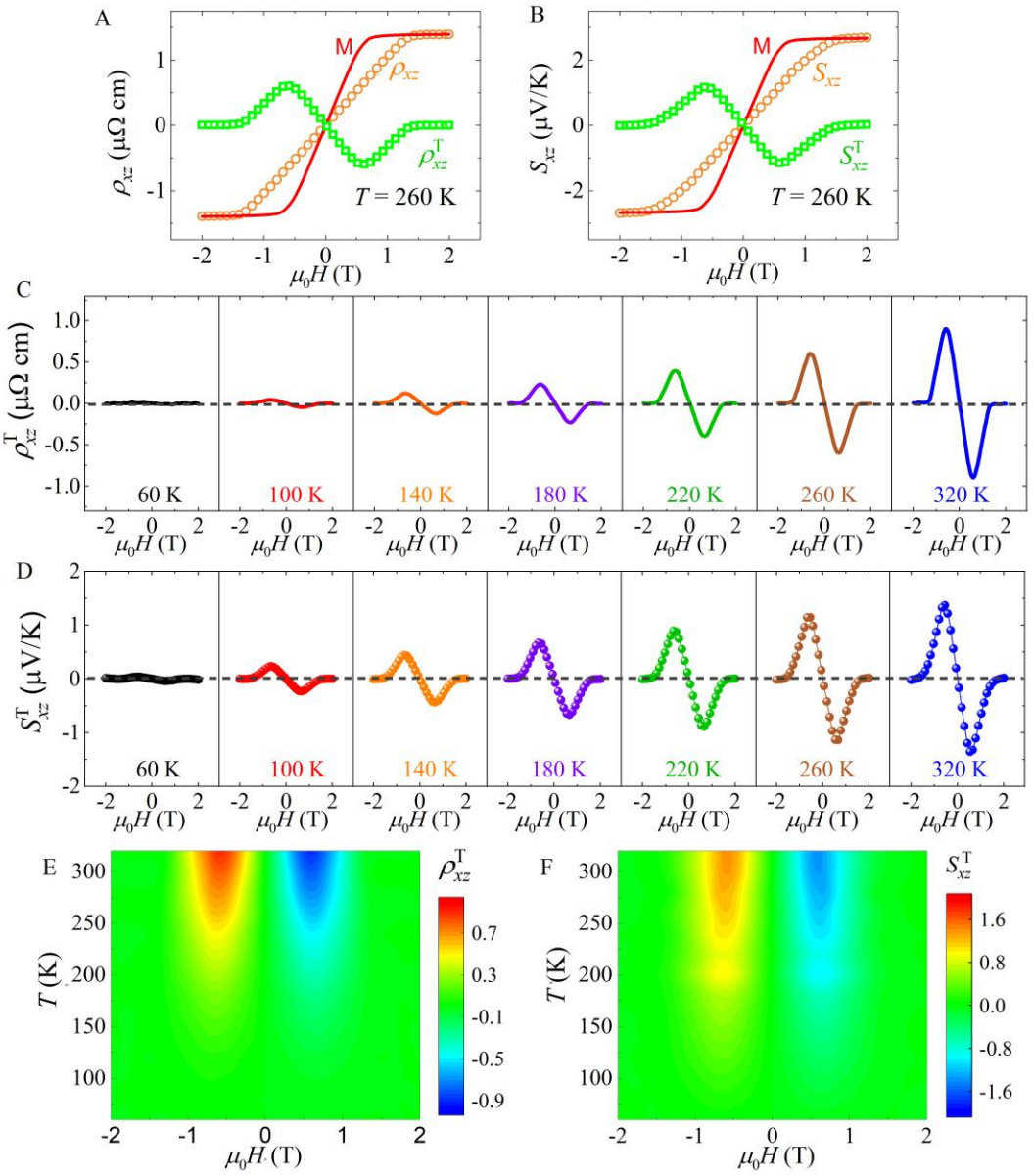

Figure 4: Topological Hall effect and topological Nernst effect. (A) Magnetic field dependence of total Hall resistivity ρ_{xz} and the scaled magnetization at 260 K. Green curve stands for the extracted topological Hall ρ_{xz}^{T} described in the main text; (B) Magnetic field dependence of total Nernst effect coefficient S_{xz} and the scaled magnetization at 260 K. Green curve stands for the extracted topological Nernst effect coefficient S_{xz}^{T}; (C) Magnetic field dependence of topological Hall ρ_{xz}^{T} at some selected temperatures. (D) The topological Nernst effect signal S_{xz}^{T} as a function of magnetic field at some selected temperatures. (E) The T-$\mu_0 H$ contour map of ρ_{xz}^{T}. (F) The T-$\mu_0 H$ contour map of S_{xz}^{T}.

Reference

1 Park, P. *et al.* Magnetic excitations in non-collinear antiferromagnetic Weyl semimetal Mn_3Sn. *npj Quantum Materials* **3**, 63, doi:10.1038/s41535-018-0137-9 (2018).

2 Wuttke, C. *et al.* Berry curvature unravelled by the anomalous Nernst effect in Mn_3Ge. *Phy. Rev. B* **100**, 085111, doi:10.1103/PhysRevB.100.085111 (2019).

3 Nayak, A. K. *et al.* Large anomalous Hall effect driven by a nonvanishing Berry curvature in the noncolinear antiferromagnet Mn_3Ge. *Sci. Adv.* **2**, e1501870, doi:10.1126/sciadv.1501 (2016).

4 Xu, G., Lian, B. & Zhang, S.-C. Intrinsic Quantum Anomalous Hall Effect in the Kagome Lattice $Cs_2LiMn_3F_{12}$. *Phys. Rev. Lett.* **115**, doi:10.1103/PhysRevLett.115.186802 (2015).

5 Lachman, E. *et al.* Exchange biased anomalous Hall effect driven by frustration in a magnetic kagome lattice. *Nat. Commun.* **11**, doi:10.1038/s41467-020-14326-9 (2020).

6 Kim, K. *et al.* Large anomalous Hall current induced by topological nodal lines in a ferromagnetic van der Waals semimetal. *Nat. Mater.* **17**, 794-799, doi:10.1038/s41563-018-0132-3 (2018).

7 Yin, J.-X. *et al.* Giant and anisotropic many-body spin–orbit tunability in a strongly correlated kagome magnet. *Nature* **562**, 91-95, doi:10.1038/s41586-018-0502-7 (2018).

8 Wu, S. *et al.* Symmetry Breaking and Ascending in the Magnetic Kagome Metal FeGe. *Phys. Rev. X* **14**, 011043, doi:10.1103/PhysRevX.14.011043 (2024).

9 Guguchia, Z. *et al.* Tunable anomalous Hall conductivity through volume-wise magnetic competition in a topological kagome magnet. *Nat. Commun.* **11**, 559, doi:10.1038/s41467-020-14325-w (2020).

10 Hollmann, N. *et al.* Electronic and magnetic properties of the kagome systems$YBaCo_4O_7$ and $YBaCo_3MO_7$(M=Al, Fe). *Phys. Rev. B* **80**, 085111, doi:10.1103/PhysRevB.80.085111 (2009).

11 Yin, J.-X. *et al.* Discovery of Charge Order and Corresponding Edge State in Kagome Magnet FeGe. *Phys. Rev. Lett.* **129**, 166401, doi:10.1103/PhysRevLett.129.166401 (2022).

12 Kurumaji, T. *et al.* Skyrmion lattice with a giant topological Hall effect in a frustrated triangular-lattice magnet. *Science* **365**, 914–918, doi:10.1126/science.aau09 (2019).

13 Yin, J.-X. *et al.* Quantum-limit Chern topological magnetism in $TbMn_6Sn_6$. *Nature* **583**, 533-536, doi:10.1038/s41586-020-2482-7 (2020).

14 Zhang, H. *et al.* Exchange-biased topological transverse thermoelectric effects in a Kagome ferrimagnet. *Nat. Commun.* **13**, 1091, doi:10.1038/s41467-022-28733-7 (2022).

15 Xu, X. *et al.* Topological charge-entropy scaling in kagome Chern magnet TbMn6Sn6. *Nature Communications* **13**, 1197, doi:10.1038/s41467-022-28796-6 (2022).

16 Ye, L. *et al.* Massive Dirac fermions in a ferromagnetic kagome metal. *Nature* **555**, 638-642, doi:10.1038/nature25987 (2018).

17 Wang, Q., Sun, S., Zhang, X., Pang, F. & Lei, H. Anomalous Hall effect in a ferromagnetic Fe_3Sn_2 single crystal with a geometrically frustrated Fe bilayer kagome lattice. *Phys. Rev. B* **94**, 075135, doi:10.1103/PhysRevB.94.075135 (2016).
18 Lin, Z. *et al.* Flatbands and Emergent Ferromagnetic Ordering in Fe_3Sn_2 Kagome Lattices. *Phys. Rev. Lett.* **121**, 096401, doi:10.1103/PhysRevLett.121.096401 (2018).
19 Liu, E. *et al.* Giant anomalous Hall effect in a ferromagnetic kagome-lattice semimetal. *Nat. Phys.* **14**, 1125-1131, doi:10.1038/s41567-018-0234-5 (2018).
20 Guin, S. N. *et al.* Zero-Field Nernst Effect in a Ferromagnetic Kagome-Lattice Weyl-Semimetal $Co_3Sn_2S_2$. *Adv. Mater.* **31**, 1806622, doi:10.1002/adma.201806622 (2019).
21 Teng, X. *et al.* Magnetism and charge density wave order in kagome FeGe. *Nat. Phys.* **19**, 814-822, doi:10.1038/s41567-023-01985-w (2023).
22 Chen, Z. *et al.* Instability of the charge density wave in the kagome magnet FeGe. *Phys. Rev. B* **110**, 245104, doi:10.1103/PhysRevB.110.245104 (2024).
23 Asaba, T. *et al.* Colossal anomalous Nernst effect in a correlated noncentrosymmetric kagome ferromagnet. *Sci. Adv.* **7**, eabf1467, doi:10.1126/sciadv.abf1467 (2021).
24 Hosur, P. & Qi, X. Recent developments in transport phenomena in Weyl semimetals. *C. R. Phys.* **14**, 857-870, doi:10.1016/j.crhy.2013.10.010 (2013).
25 Xiao, D., Chang, M.-C. & Niu, Q. Berry phase effects on electronic properties. *Rev. Mod. Phys.* **82**, 1959-2007, doi:10.1103/RevModPhys.82.1959 (2010).
26 Anomalous Nernst effect and field-induced Lifshitz transition in the Weyl semimetals TaP and TaAs. *Phy. Rev. B* **98**, 201107(R), doi:10.1103/PhysRevB.98.201107 (2018).
27 Liang, T. *et al.* Anomalous Nernst Effect in the Dirac Semimetal Cd_3As_2. *Phys. Rev. Lett.* **118**, 136601, doi:10.1103/PhysRevLett.118.136601 (2017).
28 Jia, Z. *et al.* Thermoelectric signature of the chiral anomaly in Cd_3As2. *Nat. Commun.* **7**, 13013 doi:10.1038/ncomms13013 (2016).
29 Lou, R. *et al.* Orbital-selective effect of spin reorientation on the Dirac fermions in a non-charge-ordered kagome ferromagnet Fe_3Ge. *Nat. Commun.* **15**, 9823, doi:10.1038/s41467-024-53343-w (2024).
30 Li, Z. *et al.* Anomalous Hall effect dominated by intrinsic mechanism in Fe_3Ge with hexagonal DO_{19} Kagome lattice and cubic DO_3 structure. *Appl. Phy. Lett.* **122**, doi:10.1063/5.0118768 (2023).
31 Zhang, Z. *et al.* Large topological Hall effect arising from spin reorientation in kagome magnet Fe_3Ge. *arXiv preprint arXiv* **2024** (2024).
32 Supplemental Information _ Fe_3Ge.
33 Balagurov, A. M., Samoylova, N. Y., Sumnikov, S. V., Palacheva, V. V. & Golovin, I. S. Structural and magnetic phase transitions in Fe_3Ge: A neutron diffraction study. *Phy. Rev. Mater.* **7**, 063603 doi:10.1103/PhysRevMaterials.7.063603 (2023).
34 Drijver, J. W., Sinnema, S. G. & Woude, F. Magnetic properties of hexagonal and cubic Fe_3Ge. *J. Phys. F: Met. Phys* **6**, 2165 (1976).

35 Onoda, S., Sugimoto, N. & Nagaosa, N. Intrinsic Versus Extrinsic Anomalous Hall Effect in Ferromagnets. *Phys. Rev. Lett.* **97**, 126602, doi:10.1103/PhysRevLett.97.126602 (2006).
36 Nakatsuji, S., Kiyohara, N. & Higo, T. Large anomalous Hall effect in a non-collinear antiferromagnet at room temperature. *Nature* **527**, 212-215, doi:10.1038/nature15723 (2015).
37 Li, S.-X. *et al.* Giant Anomalous Hall Effect in Kagome Nodal Surface Semimetal Fe_3Ge. *ArXiv preprint arXiv* **2501**, 12424.v12421 (2025).
38 Li, X. *et al.* Anomalous Nernst and Righi-Leduc Effects in Mn_3Sn: Berry Curvature and Entropy Flow. *Phys. Rev. Lett.* **119**, 056601 doi:10.1103/PhysRevLett.119.056601 (2017).
39 Ikhlas, M. *et al.* Large anomalous Nernst effect at room temperature in a chiral antiferromagnet. *Nat. Phys.* **13**, 1085, doi:10.1038/nphys4181 (2017).
40 Ramos, R. *et al.* Anomalous Nernst effect of Fe_3O_4 single crystal. *Phys. Rev. B* **90**, 054422 doi:10.1103/PhysRevB.90.054422 (2014).
41 Xu, L. *et al.* Anomalous transverse response of ${\mathrm{Co}}_{2}\mathrm{MnGa}$ and universality of the room-temperature ${\ensuremath{\alpha}}_{ij}^{A}/{\ensuremath{\sigma}}_{ij}^{A}$ ratio across topological magnets. *Physical Review B* **101**, 180404, doi:10.1103/PhysRevB.101.180404 (2020).
42 Miyasato, T. *et al.* Crossover Behavior of the Anomalous Hall Effect and Anomalous Nernst Effect in Itinerant Ferromagnets. *Phys. Rev. Lett.* **99**, 086602, doi:10.1103/PhysRevLett.99.086602 (2007).
43 Asamitsu, A. *et al.* Anomalous Hall effect and Nernst effect in itinerant ferromagnets. *J. Magn. Magn. Mater.* **310**, 2000-2002, doi:10.1016/j.jmmm.2006.10.691 (2007).
44 Guin, S. N. *et al.* Anomalous Nernst effect beyond the magnetization scaling relation in the ferromagnetic Heusler compound Co_2MnGa. *NPG Asia Mater.* **11**, doi:10.1038/s41427-019-0116-z (2019).
45 Hanasaki, N. *et al.* Anomalous Nernst Effects in Pyrochlore Molybdates with Spin Chirality. *Phys. Rev. Lett.* **100**, 106601, doi:10.1103/PhysRevLett.100.106601 (2008).
46 Hirokane, Y., Tomioka, Y., Imai, Y., Maeda, A. & Onose, Y. Longitudinal and transverse thermoelectric transport in MnSi. *Phys. Rev. B* **93**, 014436, doi:10.1103/PhysRevB.93.014436 (2016).
47 Smith, A. W. The Transverse Thermomagnetic Effect in Nickel and Cobalt. *Phys. Rev.* **33**, 295-306, doi:10.1103/PhysRevSeriesI.33.295 (1911).
48 Uchida, K.-i., Zhou, W. & Sakuraba, Y. Transverse thermoelectric generation using magnetic materials. *Appl. Phys. Lett.* **118**, 140504, doi:10.1063/5.0046877 (2021).
49 Zhang, H., Xu, C. Q. & Ke, X. Topological Nernst effect, anomalous Nernst effect, and anomalous thermal Hall effect in the Dirac semimetal Fe_3Sn_2. *Phys. Rev. B* **103**, L201101, doi:10.1103/PhysRevB.103.L201101 (2021).

50 Zhou, W. & Sakuraba, Y. Heat flux sensing by anomalous Nernst effect in Fe–Al thin films on a flexible substrate. *Appl. Phys. Exp* **13**, 043001, doi:10.35848/1882-0786/ab79fe (2020).
51 Sakai, A. *et al.* Iron-based binary ferromagnets for transverse thermoelectric conversion. *Nature* **581**, 53-57, doi:10.1038/s41586-020-2230-z (2020).
52 Li, M. *et al.* Large Anomalous Nernst Effects at Room Temperature in Fe3Pt Thin Films. **35**, 2301339, doi:https://doi.org/10.1002/adma.202301339 (2023).
53 Taguchi, Y., Oohara, Y., Yoshizawa, H., Nagaosa, N. & Tokura, Y. Spin Chirality, Berry Phase, andAnomalous Hall Effect in aFrustrated Ferromagnet. *Science* **291**, 30, doi:10.1126/science.1058161 (2001).
54 Ishizuka, H. & Nagaosa, N. Spin chirality induced skew scattering and anomalous Hall effect in chiral magnets. *Sci. Adv.* **4**, eaap9962, doi:10.1126/sciadv.aap996 (2018).
55 Madhogaria, R. P. *et al.* Topological Nernst and topological thermal Hall effect in rare-earth kagome $ScMn_6Sn_6$. *Phys. Rev. B* **108**, 125114, doi:10.1103/PhysRevB.108.125114 (2023).
56 Shiomi, Y., Kanazawa, N., Shibata, K., Onose, Y. & Tokura, Y. Topological Nernst effect in a three-dimensional skyrmion-lattice phase. *Phys. Rev. B* **88**, 064409, doi:10.1103/PhysRevB.88.064409 (2013).
57 Hirschberger, M. *et al.* Topological Nernst Effect of the Two-Dimensional Skyrmion Lattice. *Phys. Rev. Lett.* **125**, 076602, doi:10.1103/PhysRevLett.125.076602 (2020).
58 Xu, Y. *et al.* Unconventional Transverse Transport above and below the Magnetic Transition Temperature in Weyl Semimetal $EuCd_2As_2$. *Phys. Rev. Lett.* **126**, 076602, doi:10.1103/PhysRevLett.126.076602 (2021).
59 Kolincio, K. K. *et al.* Large Hall and Nernst responses from thermally induced spin chirality in a spin-trimer ferromagnet. *Proc. Natl. Acad. Sci. U.S.A.* **118**, 33 e2023588118, doi:10.1073/pnas.2023588118 (2021).
60 Ghimire, N. J. *et al.* Competing magnetic phases and fluctuation-driven scalar spin chirality in the kagome metal YMn₆Sn₆. **6**, eabe2680, doi:doi:10.1126/sciadv.abe2680 (2020).
61 Wang, Q. *et al.* Field-induced topological Hall effect and double-fan spin structure with a c-axis component in the metallic kagome antiferromagnetic compound $\mathrm{Y}{\mathrm{Mn}}_{6}{\mathrm{Sn}}_{6}$. *Physical Review B* **103**, 014416, doi:10.1103/PhysRevB.103.014416 (2021).
62 Fruhling, K. *et al.* Topological Hall effect induced by chiral fluctuations in ${\mathrm{ErMn}}_{6}{\mathrm{Sn}}_{6}$. *Physical Review Materials* **8**, 094411, doi:10.1103/PhysRevMaterials.8.094411 (2024).
63 Emmanuel, O. O., Gupta, S. & Ke, X. ErMn6Sn6: A Promising Kagome Antiferromagnetic Candidate for Room-Temperature Nernst Effect-Based Thermoelectrics. *Advanced Functional Materials* **n/a**, 2418715, doi:https://doi.org/10.1002/adfm.202418715.
64 Sürgers, C., Fischer, G., Winkel, P. & Löhneysen, H. v. Large topological Hall effect in the non-collinear phase of an antiferromagnet. *Nature Communications* **5**, 3400, doi:10.1038/ncomms4400 (2014).

65 Liu, Z. H. *et al.* Transition from Anomalous Hall Effect to Topological Hall Effect in Hexagonal Non-Collinear Magnet Mn3Ga. *Scientific Reports* **7**, 515, doi:10.1038/s41598-017-00621-x (2017).
66 Afshar, M. & Mazin, I. I. Spin spiral and topological Hall effect in ${\mathrm{Fe}}_{3}{\mathrm{Ga}}_{4}$. *Physical Review B* **104**, 094418, doi:10.1103/PhysRevB.104.094418 (2021).
67 Baral, P. R. *et al.* Fluctuation-driven topological Hall effect in room-temperature itinerant helimagnet Fe3Ga4. *Nature Communications* **16**, 3898, doi:10.1038/s41467-025-58933-w (2025).
68 Xu, X. (Private discussion).